Insights into Western Sicily's seismotectonics from recent seismicity and 1968 Belice mainshock ground motion simulations

Scarfì L.[1*], Barberi G.[1], Barreca G.[2], Musumeci C.[1], Tusa G.[1]

[1] Istituto Nazionale di Geofisica e Vulcanologia, Sezione di Catania - Osservatorio Etneo, Catania, Italy
[2] Dipartimento di Scienze Biologiche, Geologiche e Ambientali, Università di Catania, Sezione di Scienze della Terra, Italy
[*] Corresponding author: Luciano Scarfì, luciano.scarfi@ingv.it

Introduction

This supplementary material provides information on the techniques and analyses used in the main article.

P-wave ray path

Figure S1 illustrates the density of seismic rays (P-waves) in the studied region.
When calculating the 3D velocity model, the measurement node grid was established exploiting an important feature of the LOTOS code (Koulakov 2009), which automatically sets up the inversion mesh according to the distribution of the seismic rays. Specifically, given a regular grid step, the software is able to not install any node in the case of absence of rays, whereas in areas of higher ray number, it can increase the grid density up to the maximum value (in our case, 2 km for both the horizontal and vertical directions). The inversion solution is further controlled by smoothing parameters which reduce the difference in the final values of neighbouring nodes. The ability to build such a dense (quasi continuous) mesh is fundamental for a 'local earthquake tomography' in order to reduce the bias of the resulting models due to the grid configuration (i.e. overly large spacing between nodes to suitably image earth heterogeneities).

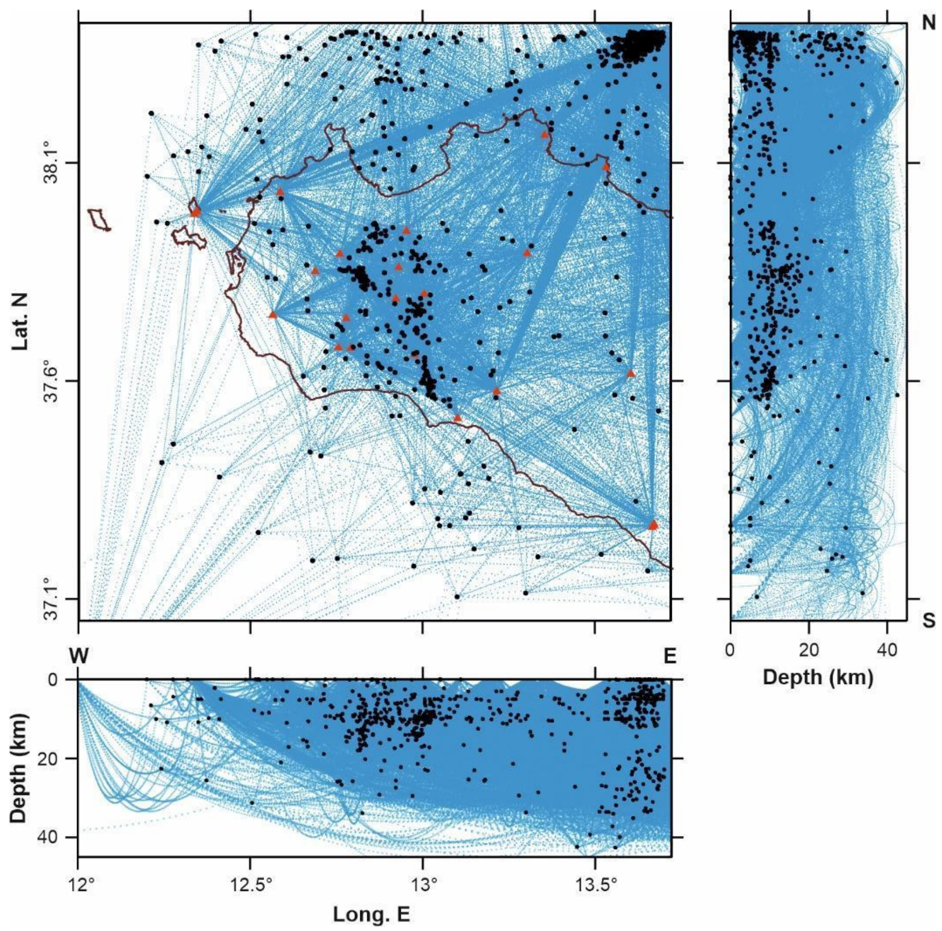

Fig. S1 P-wave ray paths traced as straight lines in the map, NS and WE sections. Red triangles and black points indicate stations and earthquakes, respectively

Synthetic tests

To evaluate the resolution limitations of our tomography, we performed a series of synthetic tests designed to reproduce an idealised velocity model (target) by inverting theoretical travel times associated with it. The synthetic model is defined as a superposition of the initial 1D velocity model and 3D anomalies of the wave velocities. To simulate picking uncertainty, we perturbed the theoretical travel times with random noise, with an average deviation of 0.1 s for both P- and S-wave data.

The recovery procedure uses the same workflow and control parameters as in the experimental data processing case. By comparing the inversion results with the target model, we can identify unrecovered areas corresponding to regions where tomographic resolution is low. This step is crucial to adequately assess the realistic resolution capacity related to the trade-off between source and velocity parameters.

Specifically, we considered traditional checkerboard models, composed of blocks with alternating positive and negative anomalies. Several checkerboard tests using different inversion grids and input anomalies of varying sizes were performed. Figure S2 shows the results obtained considering anomalies with spacing of 10 km (column A of Fig. S2), 12 km (column B) and 16 km (column C), with fluctuations of ±5% with respect to the initial velocity model, in both V_P and V_S, with opposite sign. Results show that even with the 10 km grid the dataset was able to reconstruct the checkerboard pattern in the well-sampled volume up to 12 km depth, while the 12 and 16 km grids manage to recover the anomalies in almost all areas where experimental tomographic images are interpreted, at least up to 20-30 km depth.

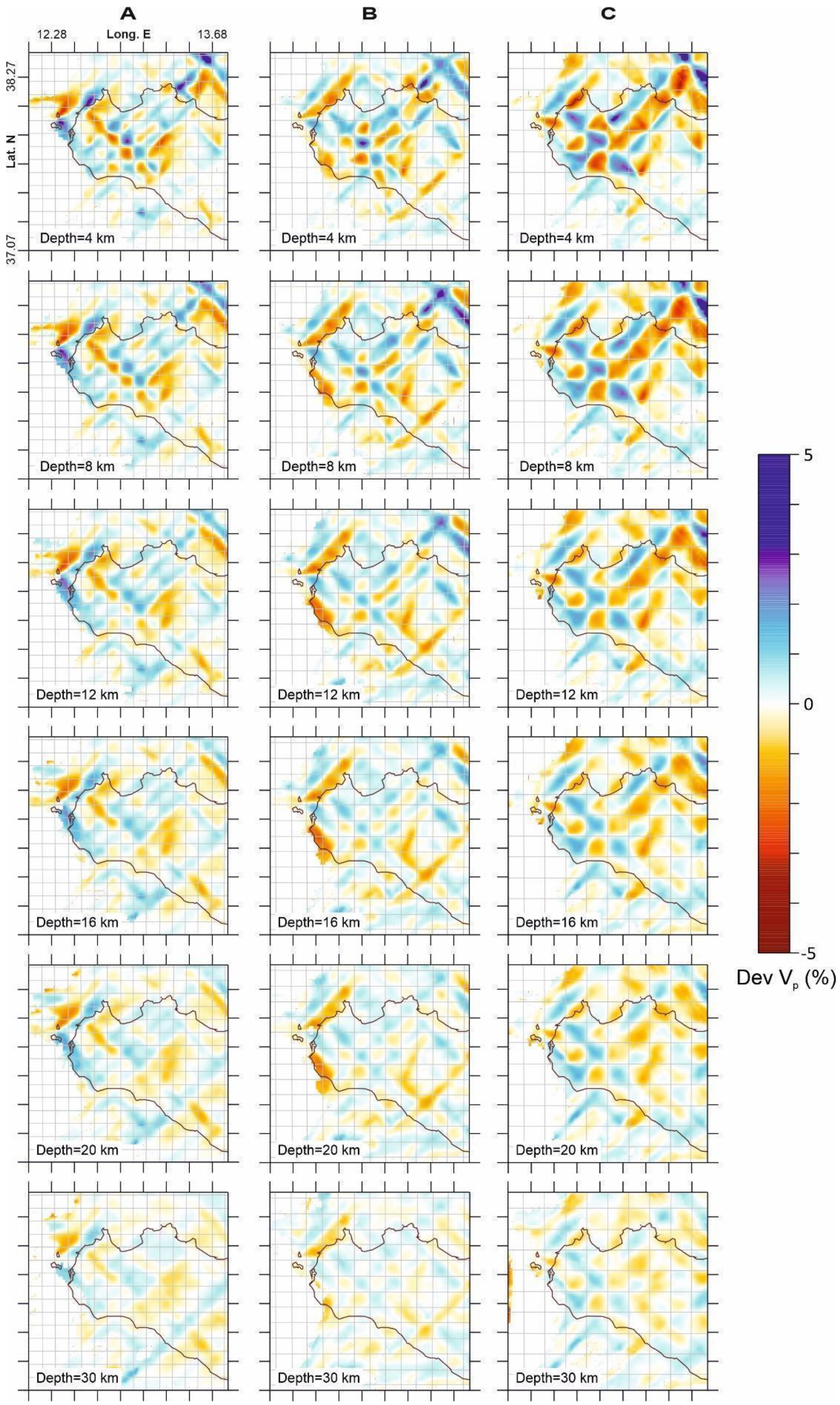

Fig. S2 Results for some representative layers of three checkerboard models having anomalies with lateral sizes of 10 km (column A), 12 km (column B) and 16 km (column C). Grey thin lines highlight the configurations of the synthetic anomalies

Focal mechanisms

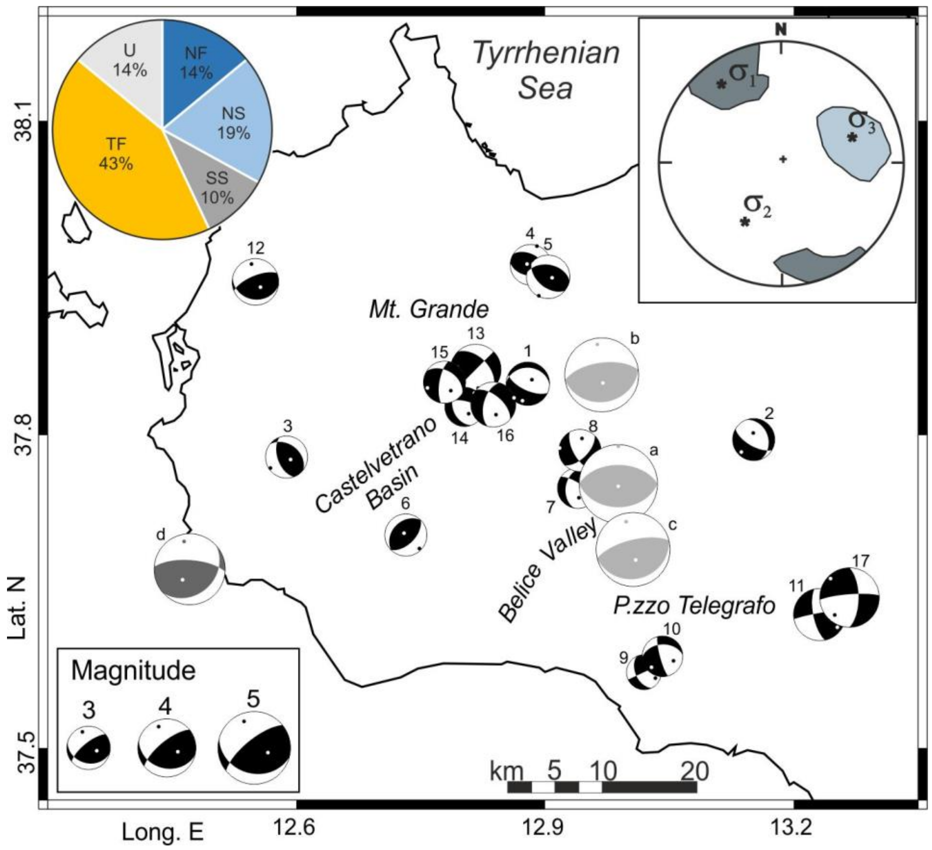

Fig. S3 Fault plane solutions (black beach balls, lower hemisphere) computed in this study, by analysing P-wave first-motion polarities. Focal mechanisms of the 1968 earthquake sequence (light grey beach balls; compressive solutions, by Anderson and Jackson 1987) and the almost pure reverse mechanism of the Mazara 1981 earthquake (dark grey beach ball, by Pondrelli and Salimbeni 2006) are also shown. The uppermost left side inset displays the occurrence of the various types of mechanisms, according to the classification by Zoback (1992): NF= Normal; NS= Normal-Strike-slip; SS=Strike-slip; TF=Reverse; U=Unknown. The inset on the right shows the lower-hemisphere projection of the principal stress-axes orientation, based on the inversion of the 18 focal mechanisms located west of long. 13.15°; grey areas indicate the 95% confidence limits of σ_1 and σ_3 orientations. The solution ID refers to Table S1

Table S1

Number, date, origin time, magnitude, hypocentral and focal parameters of the focal mechanisms computed in this study and available in the literature (A&J87 = Anderson and Jackson 1987; P&S06 = Pondrelli and Salimbeni 2006)

No	Date	Origin time	M	Lat N	Long E	Depth	PLANE1			PLANE2			P-AXIS		T-AXIS		Ref.
						km	Strike	Dip	Rake	Strike	Dip	Rake	Strike	Dip	Strike	Dip	
1	02/07/2012	19:40:36	3.0	37.848	12.878	10.4	115	65	-80	272	27	-110	45	68	198	19	This study
2	03/09/2014	05:56:27	2.9	37.794	13.151	15.3	120	65	-110	341	32	-54	356	64	225	18	This study
3	07/12/2014	05:14:43	2.9	37.777	12.587	3.5	160	55	110	308	40	64	236	8	121	72	This study
4	10/11/2016	17:53:39	2.8	37.961	12.886	3.9	95	45	70	302	48	109	19	2	282	76	This study
5	10/11/2016	18:05:56	3.0	37.954	12.887	4.1	130	50	110	280	44	68	206	3	105	74	This study
6	15/10/2017	14:16:23	2.9	37.703	12.731	9.2	45	55	90	225	35	90	135	10	315	80	This study
7	07/04/2018	19:39:23	2.8	37.758	12.974	12.8	190	40	-30	304	71	-126	173	50	60	18	This study
8	30/10/2018	01:11:58	2.9	37.766	12.971	12.8	45	60	-30	151	64	-146	10	41	277	3	This study
9	19/07/2019	06:49:13	2.4	37.574	13.021	4.8	65	90	140	155	50	0	118	27	12	27	This study
10	21/07/2019	09:41:34	2.8	37.583	13.028	2.8	165	80	-50	267	41	-165	112	41	225	24	This study
11	05/08/2019	10:16:21	3.6	37.626	13.242	9.8	260	85	20	168	70	175	32	10	126	18	This study
12	04/05/2020	17:14:37	3.2	37.945	12.549	5.4	100	25	120	248	69	77	348	22	136	64	This study
13	09/09/2020	04:56:59	3.5	37.839	12.812	10.3	45	90	40	315	50	180	172	27	278	27	This study
14	14/09/2020	03:47:02	2.7	37.843	12.794	13.6	160	40	-40	283	66	-123	149	56	36	14	This study
15	14/09/2020	03:48:01	2.9	37.845	12.796	14.0	190	70	-50	302	44	-150	143	49	252	15	This study
16	23/09/2020	20:50:11	3.1	37.840	12.815	12.5	195	55	-40	311	58	-138	165	51	72	2	This study
17	21/08/2022	04:52:49	4.1	37.633	13.247	6.6	0	65	-170	266	81	-25	220	24	315	11	This study
a	15/01/1968	02:01:08	5.4	37.750	12.983	13.0	270	50	90	90	40	90	0	5	180	85	A&J87
b	16/01/1968	16:42:44	5.1	37.857	12.976	36.0	82	27	90	262	63	90	352	18	172	72	A&J87
c	25/01/1968	09:56:48	5.1	37.687	12.966	3.0	256	69	90	76	21	90	346	24	166	66	A&J87
d	07/06/1981	13:00:56	4.9	37.670	12.470	18.0	48	29	48	274	68	110	349	21	214	61	P&S06

Stochastic simulations

Propagation path parameters

The crustal amplification function, *CA(f)*, used as input for numerical simulations has been computed considering the average 1D-shear wave velocity model reported in Table S2. The Vs-model has been derived from the 3D velocity structure of the area obtained in this study. The density values (**ρ**) of each layers have been estimated by using the empirical relation from Christensen and Mooney (1995) (through the P-wave velocities).

Table S2

1-D crustal model used to compute the crustal amplification function CA(f)

Layer top (km)	Vs (km/s)	ρ (g/cm^3)
0	2.85	2420
2	3.15	2560
4	3.32	2654
6	3.40	2704
8	3.45	2743
10	3.50	2779
12	3.60	2837
14	3.71	2892
16	3.83	2951
18	3.96	3013
20	4.09	3078
30	4.42	3268
40	4.53	3347
Half space	4.60	3485

Vs is the S-wave velocity

ρ is the density

Therefore, based on the soil classes, we assigned different site amplification curves (and high-frequency amplification decays (κ_0), according to the findings by Pischiutta et al. (2021; see Fig. S4). The site amplification curve, *SA(f)*, has been assigned on the basis of the soil classes according to the findings by Pischiutta et al. (2021). In particular, the authors generated the site amplification curves for soil classes A and D, considering a typical velocity profile for Italian soft rocks (limestones, marls and flysch), and used the ones proposed by Boore and Joyner (1997) for sites B and C (see Pischiutta et al. 2021 for major details). In Fig. S4, we show the four curves representing the product of the functions *SA(f)* and *D(f)* for the different soil classes.

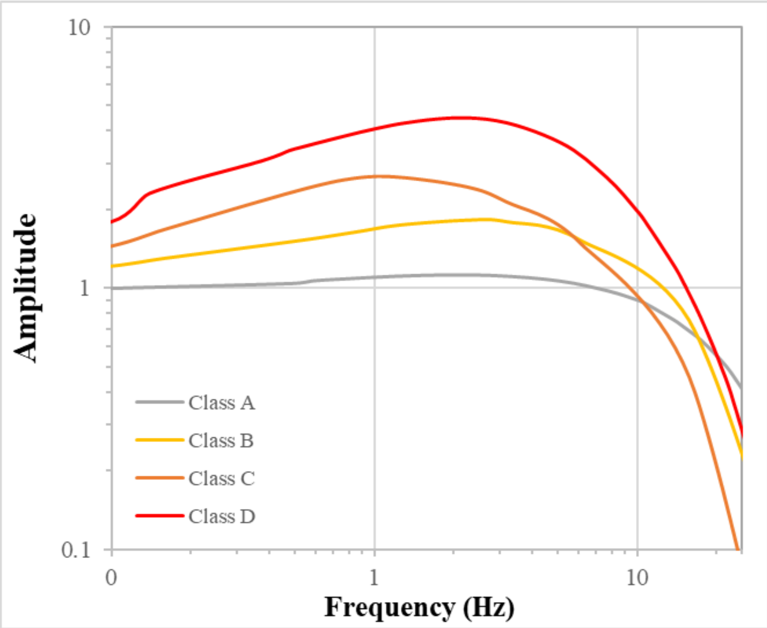

Fig. S4 Site amplifications curves, *SA(f)*, including the high-cut filter function, *D(f)*, for different values of the κ_0 filter

References

Anderson H, Jackson J (1987) Active tectonics of the Adriatic Region. Geophys J Int 91(3):937-983. https://doi.org/10.1111/j.1365-246X.1987.tb01675.x

Boore DM, Joyner WB (1997) Site amplifications for generic rock sites. Bulletin of the Seismological Society of America 87(2):327-341. https://doi.org/10.1785/BSSA0870020327

Christensen NI, Mooney WD (1995) Seismic velocity structure and composition of the continental crust: A global view. J Geophys Res Solid Earth 100(B6):9761-9788. https://doi.org/10.1029/95JB00259

Koulakov I (2009) LOTOS Code for Local Earthquake Tomographic Inversion: Benchmarks for Testing Tomographic Algorithms. Bulletin of the Seismological Society of America 99(1):194-214. https://doi.org/10.1785/0120080013

Pischiutta M, Akinci A, Tinti E, Herrero A (2021) Broad-band ground-motion simulation of 2016 Amatrice earthquake, Central Italy. Geophys J Int 224(3):1753-1779. https://doi.org/10.1093/gji/ggaa412

Pondrelli S, Salimbeni S (2006) Italian CMT Dataset [Data set]. Istituto Nazionale di Geofisica e Vulcanologia (INGV). https://doi.org/10.13127/rcmt/italy

Zoback ML (1992) First- and second-order patterns of stress in the lithosphere: The World Stress Map Project. J Geophys Res Solid Earth 97(B8):11703-11728. https://doi.org/10.1029/92JB00132